PNAS

Supporting Information for

Direct Optical Observation of Solid Electrolyte Interphase Formation Dynamics in Lithium-ion Batteries

Wenlong Li[1,†], Tianxiao Sun[1,†], Sameep Rajubhai Shah[2,†], Zhengyu Ju[1], Jigang Zhou[3], Kejie Zhao[2,*], Guihua Yu[1,*], Yijin Liu[1,*]

[1]Materials Science and Engineering Program and Walker Department of Mechanical Engineering, The University of Texas at Austin, Austin, TX 78712, USA

[2]School of Mechanical Engineering, Purdue University, West Lafayette, IN 47907, USA

[3]General Motors Company, Warren, MI 48092, USA

[†]These authors contributed equally to this work.

[*]Corresponding authors: Kejie Zhao, Guihua Yu, Yijin Liu.

Emails: kjzhao@purdue.edu, ghyu@austin.utexas.edu, and liuyijin@utexas.edu

This PDF file includes:

Supporting text
Figures S1 to S28
Tables S1 to S3
SI References

Other supporting materials for this manuscript include the following:

Movies S1 to S3

1. Refractive index matching effect: theory and validation

Refractive index matching effect refers to the reduction of Fresnel reflection at an interface when two adjacent media have similar refractive indices.(1) In optical microscopy, the reflected intensity strongly depends on the refractive-index contrast between materials: a large mismatch produces strong reflection, whereas closely matched indices minimize reflection.

In optical microscopy, for normal incidence (polarization effects being negligible), the reflectance R at an interface between two media with refractive indices n_1 and n_2 is given by the Fresnel equation:

$$R = \left(\frac{n_1 - n_2}{n_1 + n_2}\right)^2$$

Under optical microscopy, taking the observation of a graphite electrode in air as an example, with air (n≈1.0) and graphite (n≈2.7–3.0, here taken as 2.7)(2, 3).

Air–Graphite interface:

$$R = \left(\frac{2.7 - 1}{2.7 + 1}\right)^2 = 0.21$$

The calculations show that the bare air–graphite interface yields a pronounced reflectance (~21%) owing to the large refractive-index mismatch.

As a representative solid-electrolyte interphase (SEI) constituent, Li_2CO_3 (n≈1.41–1.45,(4) here taken as 1.4) was considered. When a layer of Li_2CO_3 powders is deposited on the graphite surface:

Air–Li_2CO_3 interface:

$$R = \left(\frac{1.4 - 1}{1.43 + 1}\right)^2 = 0.03$$

Li_2CO_3–Graphite interface:

$$R = \left(\frac{2.7 - 1.4}{2.7 + 1.4}\right)^2 = 0.10$$

With the deposition of a Li_2CO_3 layer on the surface of graphite, the reflection is redistributed into two weaker interfaces (~3% and ~10%). As an intermediate refractive-index medium, the Li_2CO_3 layer mitigates the optical impedance mismatch, leading to suppressed Fresnel reflection and, consequently, the overall reflected intensity is expected to be markedly reduced in optical microscopy.

To experimentally validate the refractive index matching effect, a graphite electrode was placed under an optical microscope (the experimental setup is shown in Fig. S1), and Li_2CO_3 was tested. Optical microscopy images of the pristine graphite electrode were first acquired, after which a pipette loaded with Li_2CO_3 powders was used to disperse the powders onto the electrode surface, followed by additional imaging. Subsequent optical images captured the reflectivity changes. The entire procedure was completed within one minute to minimize environmental disturbance and rule out experimental artifacts.

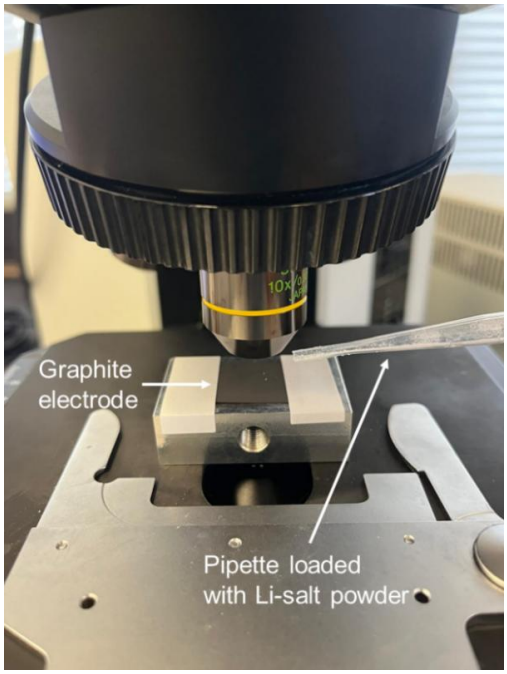

Fig. S1. Experimental setup for validating refractive index matching effect.

As shown in Fig. S2, the deposition of Li_2CO_3 powders on the graphite electrode surface leads to a pronounced reduction in optical reflectivity, manifested as darker contrast in the optical images. In Fig. S2, Li_2CO_3 dispersion causes significant darkening of the surface (Fig. S2a and Fig. S2b), with the differential map highlighting widespread blue regions that indicate decreased reflectivity. The corresponding intensity histograms show a peak shift toward lower values after Li_2CO_3 deposition, confirming an overall decline in surface resolution (Fig. S2c), while line profiles taken along the diagonal direction reveal a systematic reduction in intensity across the entire field of view (Fig. S2d). Besides Li_2CO_3, two other representative inorganic SEI constituents (Li_2O and LiOH) were tested. Similar effects are observed for Li_2O and LiOH dispersions in Figs. S3 and S4, where the graphite surface also exhibits darker contrast and extended blue regions in the differential maps, marking reduced reflectivity; in all cases, red features correspond to agglomerated salt particles, which represent the optical signal of the salt particles rather than uniform coverage of the graphite surface.

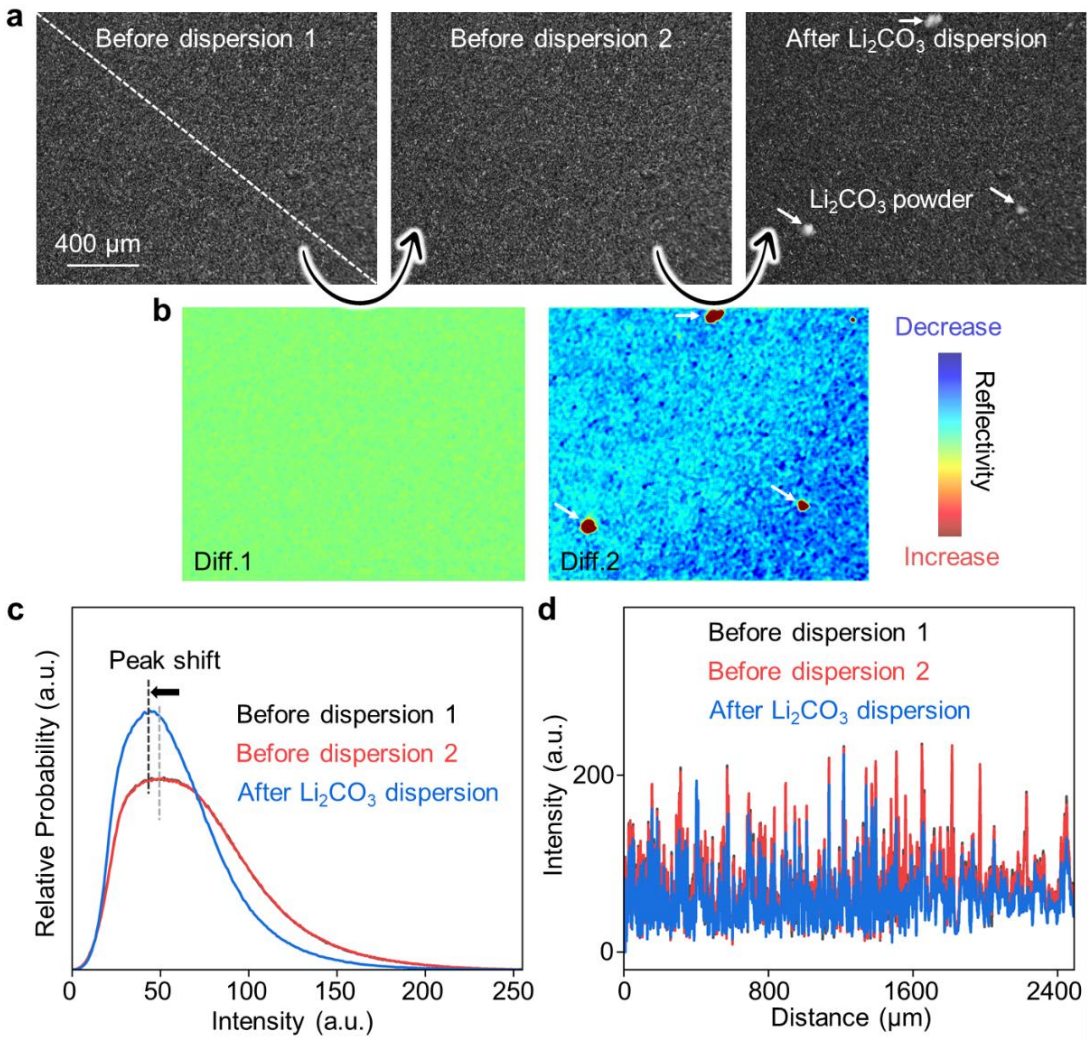

Fig. S2. Influence of Li_2CO_3 powder dispersion on the graphite electrode surface. a, Optical microscopy images of the graphite surface before and after Li_2CO_3 powder dispersion. b, Corresponding differential maps showing reflectivity variations induced by Li_2CO_3 powder. Blue regions denote areas of the graphite surface covered by a thin Li_2CO_3 layer, whereas red features indicate the presence of Li_2CO_3 powder agglomerates. c, Evolving intensity histogram of the graphite surface, derived from the three images in Fig. S2a. d, Intensity evolution derived from the three images in Fig. S2a, measured along the diagonal from the top-left (0 μm) to the bottom-right.

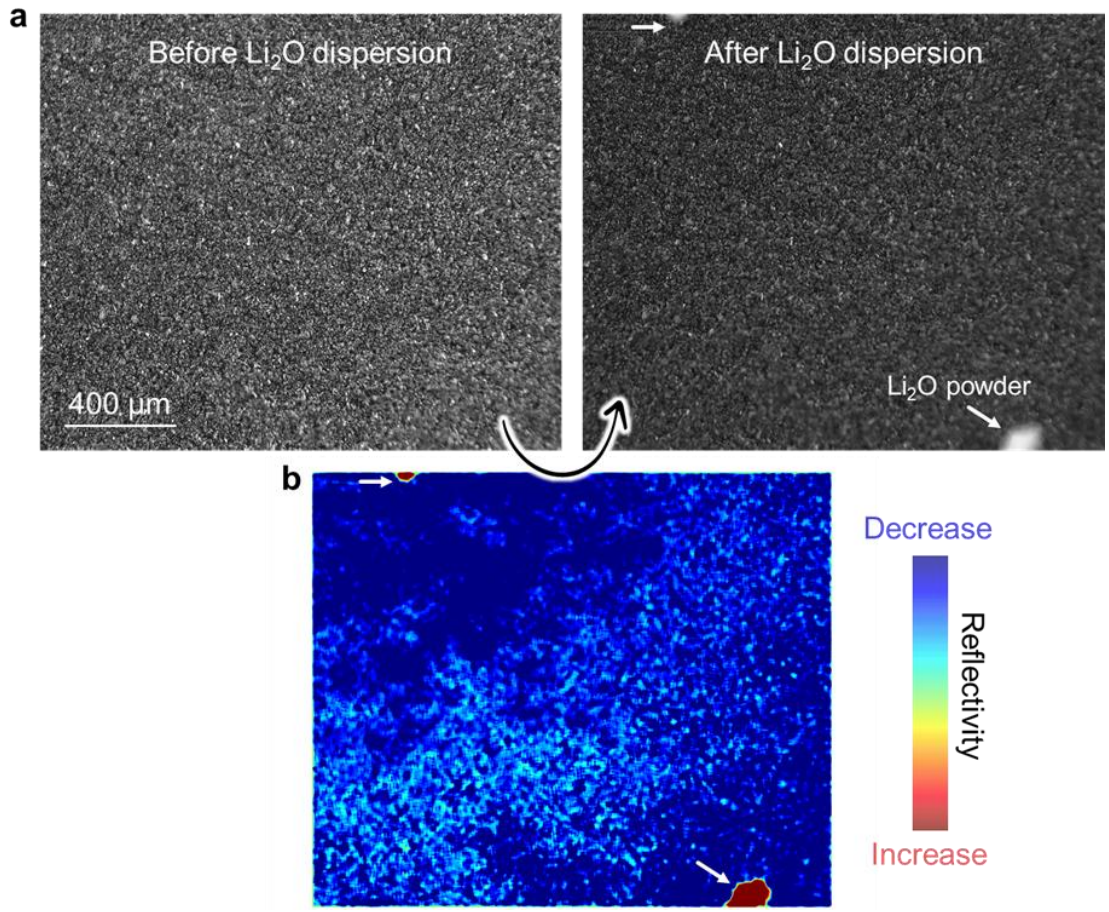

Fig. S3. Influence of Li_2O powder dispersion on the graphite electrode surface. a, Optical microscopy images of the graphite surface before and after Li_2O powder dispersion. b, The corresponding differential map showing reflectivity variations induced by Li_2O powder. Blue regions denote areas of the graphite surface covered by a thin Li_2O layer, whereas red features indicate the presence of Li_2O powder agglomerates.

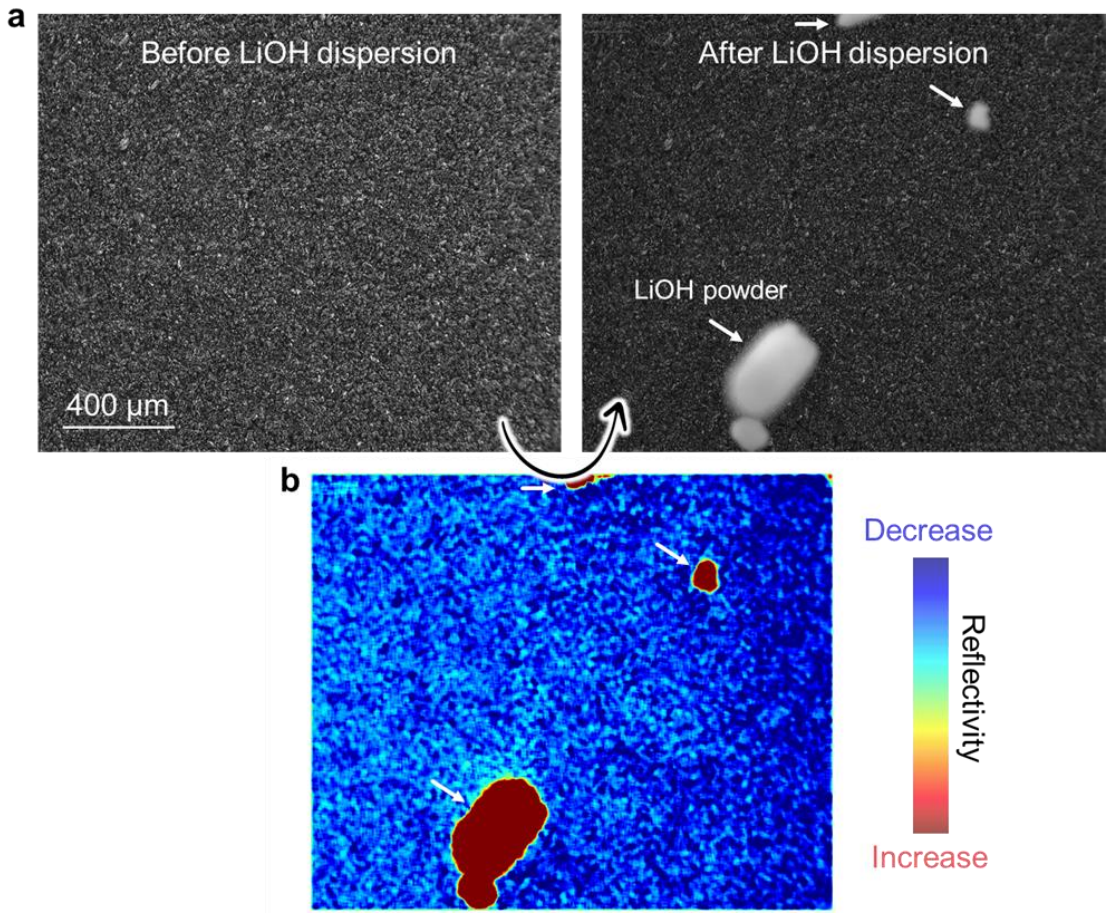

Fig. S4. Influence of LiOH powder dispersion on the graphite electrode surface. a, Optical microscopy images of the graphite surface before and after LiOH powder dispersion. b, The corresponding differential map showing reflectivity variations induced by LiOH powder. Blue regions denote areas of the graphite surface covered by a thin LiOH layer, whereas red features indicate the presence of LiOH powder agglomerates.

The SEI in lithium-ion batteries is typically only 2–10 nm thick(5), far below the ~100 nm scale (λ/4 for visible light, λ≈500–600 nm) required for significant thin-film interference(1). At such small thicknesses, the phase delay across the SEI is well below 2π, making interference negligible. In addition, while certain SEI constituents (e.g., Li_2CO_3, polymeric species) exhibit absorption in the ultraviolet, their absorption in the visible range is weak, and optical absorption is thus not considered. The refractive index (n) of the SEI in lithium ion batteries has been reported to fall within n≈1.41–1.52,(6) consistent with its major constituents including Li_2CO_3 (n≈1.41–1.45)(4), LiF (n≈1.39)(7), and organic polymeric species (n≈1.45–1.55)(8). Crucially, this range closely matches that of common electrolytes (n≈1.40)(9). With thin-film interference and absorption excluded, the reduction in reflectivity is most reasonably attributed to refractive index matching between the electrolyte and the SEI. Moreover, the SEI also serves as an intermediate optical layer that alleviates the large refractive-index mismatch between the electrolyte and graphite (n≈2.7). As a result, the overall reflected intensity is markedly suppressed, and the graphite surface appears darker under optical microscopy once covered by the SEI.

2. Operando optical microscopy setup and validation

In-situ optical measurements were performed using modified CR2016-type coin cells equipped with a transparent glass window, allowing direct observation of the electrode surface. For graphite/lithium metal half-cell studies, graphite electrodes were punched to 10 mm in diameter and paired with Li metal counter electrodes. For full-cell studies, 14 mm $LiFePO_4$ (LFP) cathodes and 12 mm graphite anodes were used, corresponding to an N/P ratio of ~1.1. Polypropylene (PP) separators were pre-soaked in 1 M $LiPF_6$ in EC/DEC (1:1 v/v) electrolyte prior to assembly, with no additional electrolyte introduced into the optical cells.

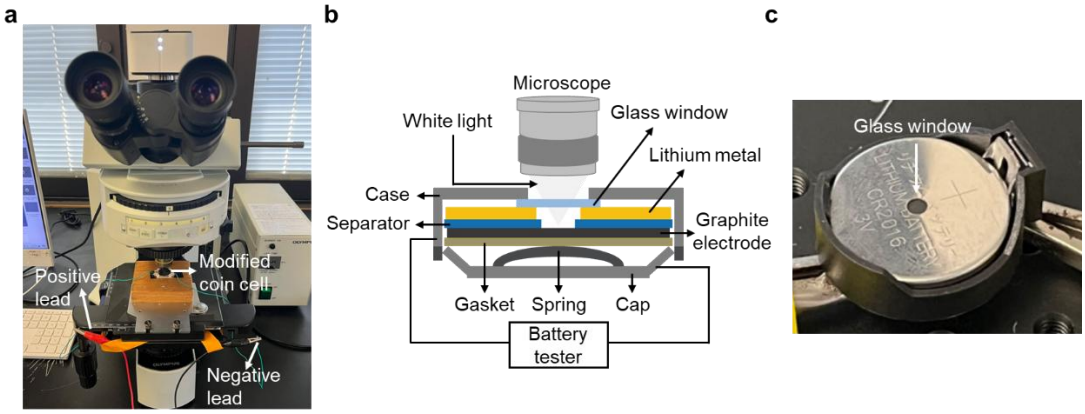

Fig. S5. a, Experimental setup for in situ optical microscopy with a modified CR2016 coin cell. b, Schematic illustration of the optical microscopy setup for operando observations of reaction dynamics in the graphite electrode. c, Modified CR2016 coin cell used in optical experiments.

The assembled cells were mounted on an Olympus BX51 optical microscope connected to a computer for automated image acquisition, which was simultaneously linked to a BioLogic VMP3 workstation for synchronized electrochemical control. Images were acquired at 10× or 20× magnification with user-defined intervals of 10 s or 1 min, enabling continuous monitoring for tens of hours. Electrochemical protocols included galvanostatic cycling of graphite/Li half-cells at C/20 and C/10 (0.01–2V), and LFP/graphite full cells at 1C (2.5–4V). In all cases, the imaging field of view was focused on the graphite electrode surface to monitor SEI evolution.

Optical microscopy has previously been employed to study graphite electrodes during electrochemical cycling, where the optical response to lithiation as a function of state of charge (SOC) has been well documented. Specifically, graphite exhibits a progressive colour transition from black, through red, to gold as its lithium content increases.(10) This is in good agreement with our ex-situ observation of the graphite electrodes recovered from the cells at different SOC (Fig. S6). However, under our operando reflection-mode optical microscopy, SOC-dependent colour transitions are inherently absent, since this imaging geometry does not render such changes (Fig. S7). Instead, the primary optical response is a darkening of surface reflectance. The darkening phenomenon observed in our operando optical experiment is clearly unrelated to the SOC. It occurs only during the first lithiation and remains irreversible even after multiple subsequent charge–discharge cycles (Fig. S8). Moreover, this phenomenon is clearly driven by electrochemical reactions as no change was observed in a control cell that was not subjected to the charging current (Fig. S9).

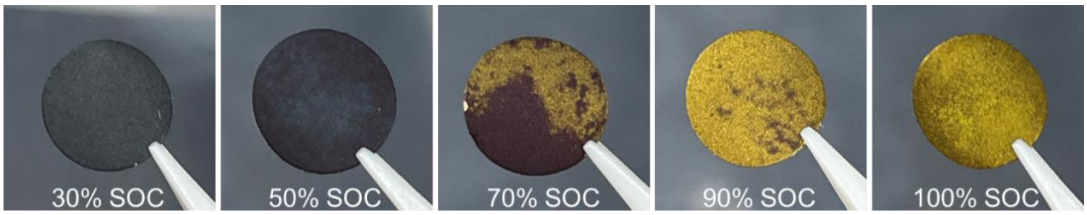

Fig. S6. Macroscopic (camera-view) images of graphite electrodes at different SOCs showing pronounced colour evolution. Diameter of each electrode: 10 mm.

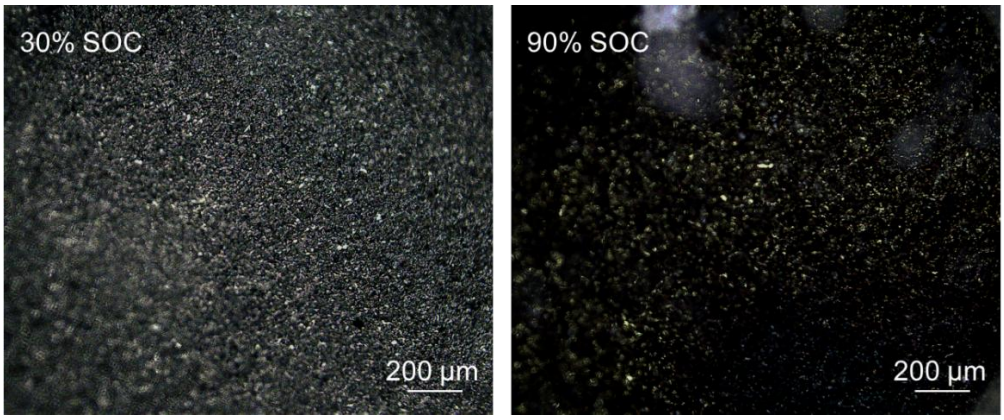

Fig. S7. Optical microscopy views of graphite electrodes at different SOCs (30% and 90%) in reflection mode.

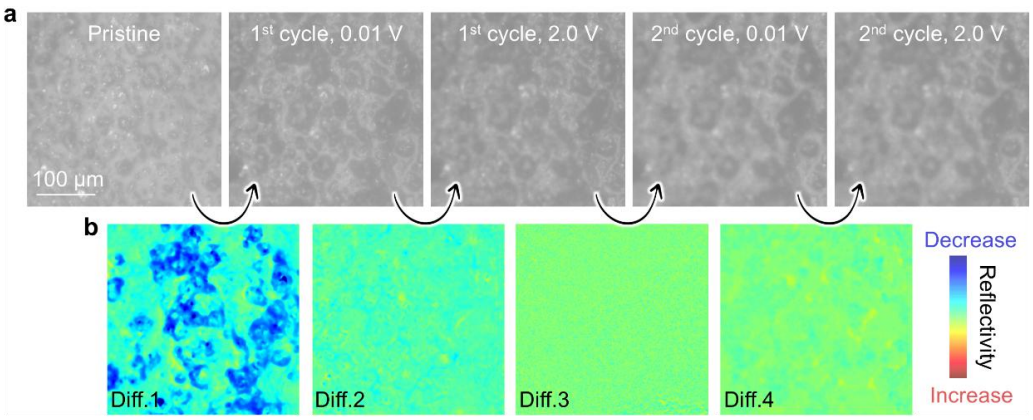

Fig. S8. Surface evolution of the graphite electrode during cycling in the graphite/Li metal half-cell at C/10 within 0.01–2.0 V, revealed by optical and differential imaging. a, Optical microscopy at the pristine state and the voltage end points of the 1st and 2nd cycles. b, Sequential differential maps highlighting the active regions on the graphite electrode surface. Pronounced changes are only observed at 0.01 V in the 1st cycle.

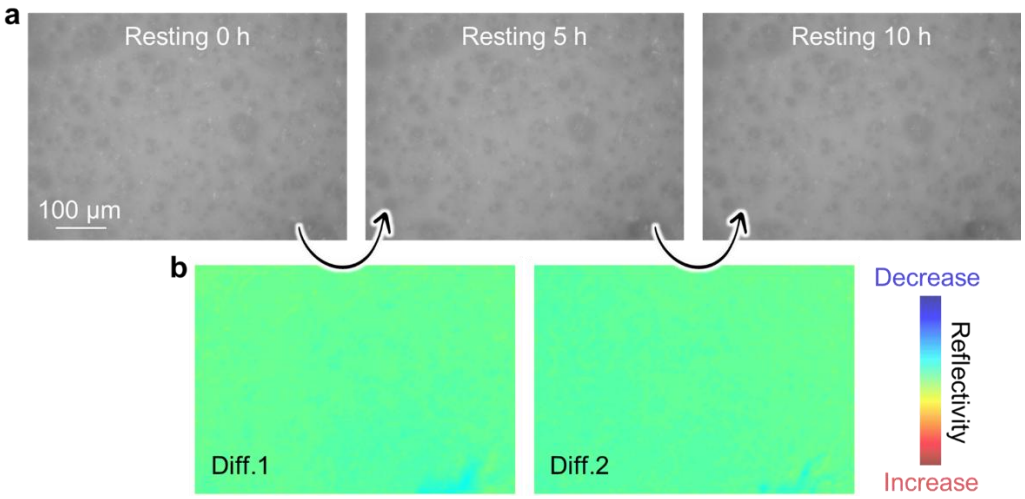

Fig. S9. Surface stability of the graphite electrode in the graphite/Li metal half-cell during rest (no current), revealed by optical and differential imaging. a, Optical microscopy images at different resting times. b, Differential maps evidencing minimal changes.

3. Surface chemical transformations correlated with optical reflectivity reduction

Ex situ SEM/EDX and XPS analyses before and after the first lithiation confirmed electrolyte decomposition and SEI formation on graphite, revealing the emergence of LiF, Li_2O, LiOH, Li_2CO_3 and $ROCO_2Li$. These surface chemical transformations are consistent with our operando optical observations, validating that the observed image darkening arises from SEI growth.

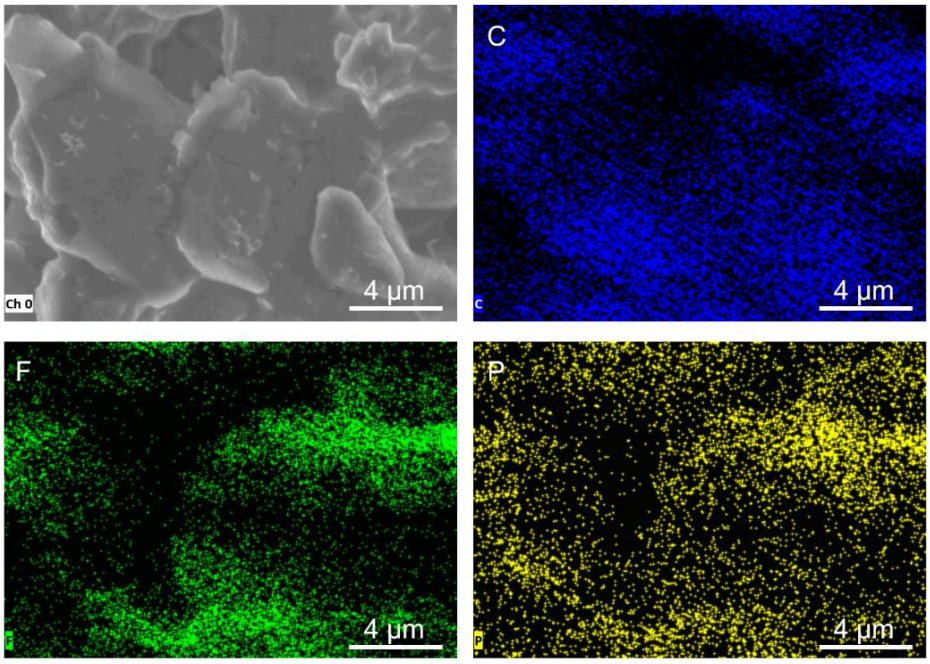

Fig. S10. EDX elemental C, P and F mapping of the pristine graphite electrode soaked in electrolyte (1.0 M $LiPF_6$ in EC/DEC = 50/50 (v/v)) prior to the first lithiation.

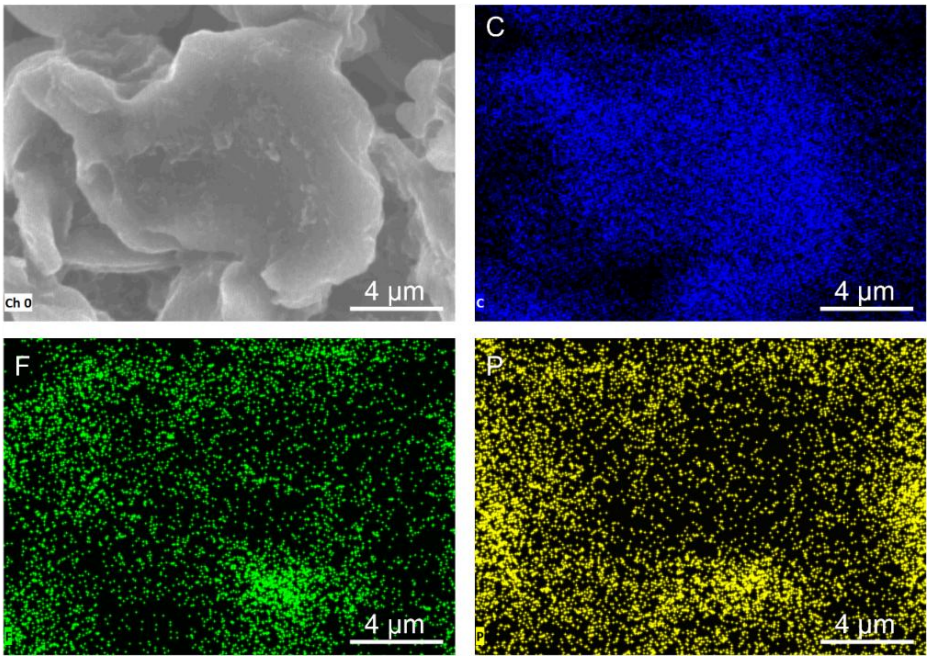

Fig. S11. EDX elemental C, P and F mapping of graphite electrode after the first lithiation to 0.01 V.

4. Detailed spatiotemporal mapping of SEI growth under different currents

Operando optical imaging under different charging currents reveals distinct SEI formation kinetics. At C/20, SEI develops sequentially and locally with isolated reaction fronts (Fig. S12); at C/10, nucleation occurs more rapidly at multiple discrete sites (Fig. S13); and at 1C, SEI forms concurrently across broader regions (Fig. S14). The corresponding electrochemical data are provided in Supplementary Fig. S15.

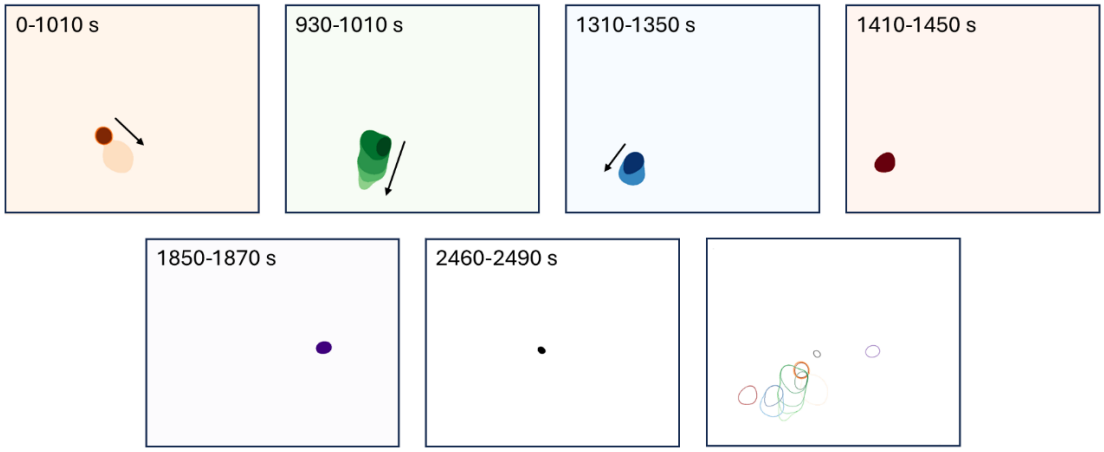

Fig. S12. Localized spatiotemporal evolution of SEI formation at C/20 in a graphite/Li metal half-cell, with individual regions extracted from the final contour map of Fig. 3a.

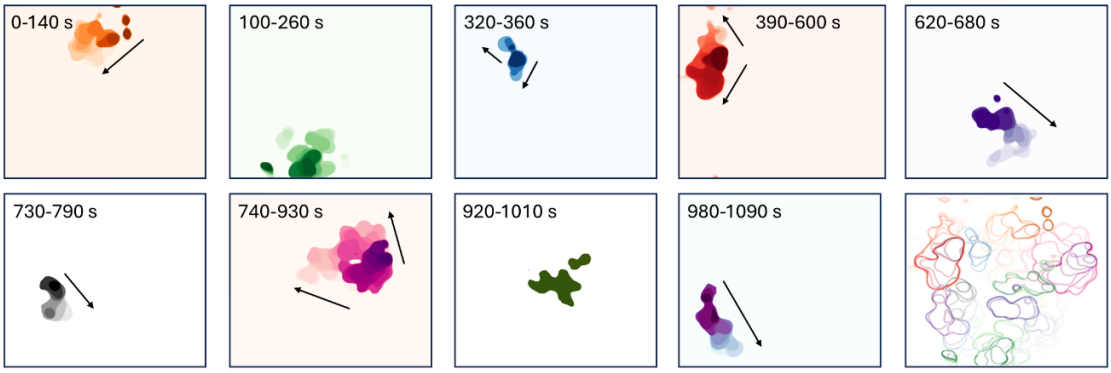

Fig. S13. Localized spatiotemporal evolution of SEI formation at C/10 in a graphite/Li metal half-cell, with individual regions extracted from the final contour map of Fig. 3b.

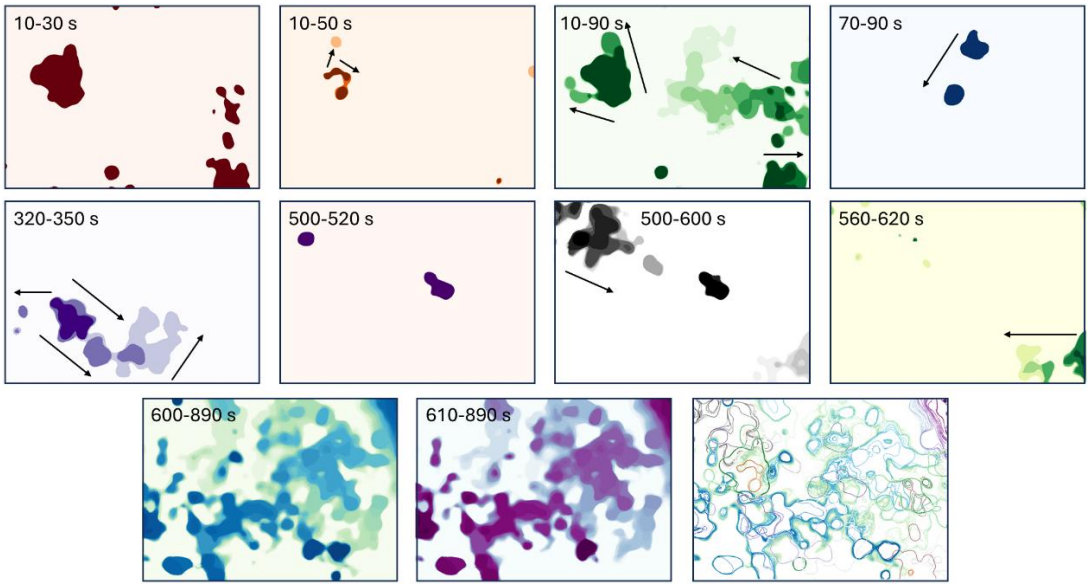

Fig. S14. Localized spatiotemporal evolution of SEI formation at 1C in a LFP/graphite coin cell, with individual regions extracted from the final contour map of Fig. 3c.

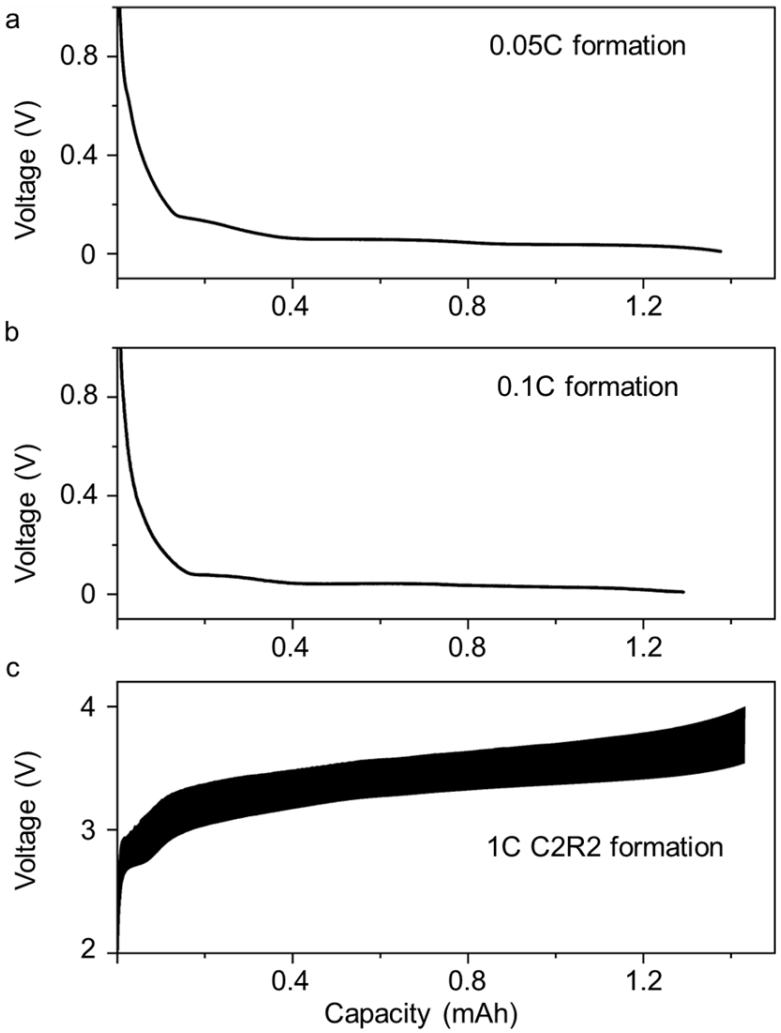

Fig. S15. Electrochemical data of the first lithiation/charge: a, graphite/Li metal half-cell at C/20; b, graphite/Li metal half-cell at C/10; c, LFP/graphite full cell at 1C pulse current structure.

5. Finite element modelling of SEI nucleation and growth

During the lithiation process, intercalation of bare Li^+ ions into the graphene layers is the ideal desired outcome. However, it is well known that Li^+ intercalation happens at lower anode potentials vs Li/Li^+. The electrochemical potential (and the Fermi level) of the anode varies during lithiation, simultaneously along with changing Li content. Electrolyte reduction reactions can occur when anode electrochemical potential exceeds the last unoccupied molecular orbital (LUMO) of the electrolyte.(11) Side reactions such as co-intercalation of solvent molecules coordinated with Li^+ ions and the consequent solvent decomposition, heterogeneous electron transfer from graphite to solvent molecules, and heterogeneous electron transfer from graphite to salt anions are more prevalent during higher potential periods.(12) A result of these side reactions is the formation of insoluble reduction reaction products – the first step in the formation of SEI film. The free energy change for the reduction process (ΔG_R) via a variety of pathways, is generally mathematically embedded into the SEI reaction driving force – SEI overpotential, η_{SEI} (Eq. 1), in the form of electrolyte reduction potential, E_{SEI}. SEI formation initiates when the electrode potential, E drops under E_{SEI}.

$$\eta_{SEI} = E - E_{SEI} - E_{nuc} - i_{SEI}R_{SEI} \quad (1)$$

The second step in SEI formation involves the precipitation of a portion of insoluble reduction products under certain conditions, generally following nucleation mechanism. The precipitation of insoluble reduction reaction products and nucleation of SEI species islands on the electrode surface involves an energy barrier, with the free energy change for this precipitation-nucleation process denoted as ΔG_{nuc} .(12-14) ΔG_{nuc} is decomposed into components proportional to the volume and surface of the solid phases ($\Delta_V G$ and $\Delta_S G$, respectively):

$$\Delta G_{nuc} = \Delta_V G + \Delta_S G \tag{2}$$

A balance between $\Delta_V G$ and $\Delta_S G$ defines a critical volume of the precipitated solid particle under which the particle is under unstable equilibrium and tends to redissolve into the electrolyte solution. Particles above the critical volume threshold have gradually decreasing ΔG_{nuc} with increasing volume, indicating a higher tendency for SEI nucleation and growth. Moreover, the presence of graphite surface can alter the nucleation process. The nucleation of SEI species on the graphite surface includes partial destruction or replacement of the graphite–electrolyte interface. The resulting release of excess free energy ($\Delta_{S,D} G$) partially compensates for the free energy required for the creation of new SEI–electrolyte and SEI–graphite interfaces ($\Delta_{S,C} G$) such that $\Delta_S G$ can be further decomposed as

$$\Delta G_{nuc} = \Delta_V G + \Delta_{S,C} G + \Delta_{S,D} G \tag{3}$$

$$\Delta G_{nuc} = \int \Gamma \, dV + \int \gamma_{SEI|El} \, dS_{SEI|El} + \int \gamma_{SEI|Gr} \, dS_{SEI|Gr} - \int \gamma_{Gr|El} \, dS_{Gr|El} \tag{4}$$

where V is the volume of the solid particle $S_{SEI|El}$, $S_{SEI|Gr}$, and $S_{Gr|El}$, represent the SEI solid particle – electrolyte interface, SEI solid particle – graphite interface and the graphite – electrolyte interface, respectively. A positive sign represents newly created interfaces while a negative sign represents destructed interface. The supersaturation potential, Γ is the lowered free energy for unit transfer of SEI species from the electrolyte solution to the interior of the SEI solid particle. $\gamma_{SEI|El}$, $\gamma_{SEI|Gr}$, and $\gamma_{Gr|El}$ are the specific interface free energies that translate to the free energy increase in creation of unit area of their respective interface. Furthermore, the presence of previously nucleated SEI island on the graphite surface can further alter the surface components of the nucleation energy barrier ($\Delta_{S,C} G$ and $\Delta_{S,D} G$).(14) The reduction reaction described as the first step in SEI formation are more responsible for governing the chemical composition of the SEI species on graphite surface while the nucleation mechanism (second step in SEI formation) governs the structural composition of the SEI layer. Spatially varying electrolyte solution composition, graphite grain orientation, localized reduction reactions, and local saturation level in the electrolyte result in a spatially inhomogeneous reduction reaction energy barrier, resulting in a mosaic of SEI species. These factors contribute to spatial dependence of Γ. Additionally, spatially varying graphite grain orientations, local Li content, and spatiotemporally evolving preexisting SEI nuclei species, ensure a spatial dependence of the specific interface free energies ($\gamma_{SEI|El}$, $\gamma_{SEI|Gr}$, and $\gamma_{Gr|El}$) that govern the nucleation process for each new SEI island. This spatial variation in the SEI formation processes is lost in modeling approaches that consider a constant reduction potential, E_{SEI} for SEI formation. To capture the spatial variation in SEI formation and nucleation, a spatially dependent potential $E_{nuc}(X)$ is included in the SEI overpotential as described in Eq. 1.

Build-up of numerous SEI nuclei of varying composition and sizes together, forms the SEI film. As the reduction reactions proceed with additional SEI nuclei being formed, the SEI film continues to grow in thickness until the transport losses across the SEI are large enough to limit further growth. Due to spatial inhomogeneity in the formation and nucleation process, combined with species specific formation potentials, it is generally observed that the SEI film consists of an inner dense layer composed primarily of inorganic species, and an outer porous layer composed of organic species.

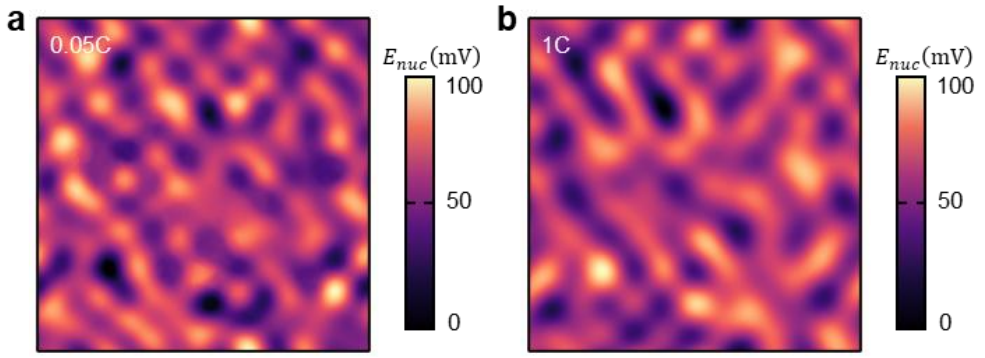

Fig. S16. Spatial variation of SEI nucleation potential E_{nuc} used in finite element SEI formation and growth simulations at a, C/20 and b, 1C, for a graphite/Li metal half-cell.

6. Characterization of LIBs after formation and ageing cycling

Building on the finding that higher current promotes more synchronized SEI development across the electrode, we next evaluated high-current formation strategies in LFP/graphite full cells. To link electrochemical performance with interfacial properties, we conducted systematic post-formation and post-aging characterizations of these cells.

6.1 Characterization of LIBs after formation

First, electrochemical impedance spectroscopy (EIS) was performed on a Biologic SP-300 electrochemical workstation, with spectra recorded over a frequency range of 100 kHz to 100 mHz using a 5 mV AC perturbation. All measurements were carried out at room temperature in a two-electrode configuration with the cell directly connected to the instrument. EIS measurements (Fig. S17 and Table S1) show that after the formation cycle, the cell formed under the 1C C2R2 protocol exhibits the lowest interfacial resistance (R_{SEI} = 2.53 Ω), and the cell under 0.1C formation exhibits the highest resistance (R_{SEI} = 5.61 Ω). After the first 1C cycle, R_{SEI} values decrease across all cells, with the 1C C2R2 cell maintaining the lowest interfacial resistance (2.38 Ω) compared to 3.52 Ω for 0.1C and 3.48 Ω for 1C. These results indicate that pulsed high-current formation effectively reduces and sustains lower interfacial resistance.

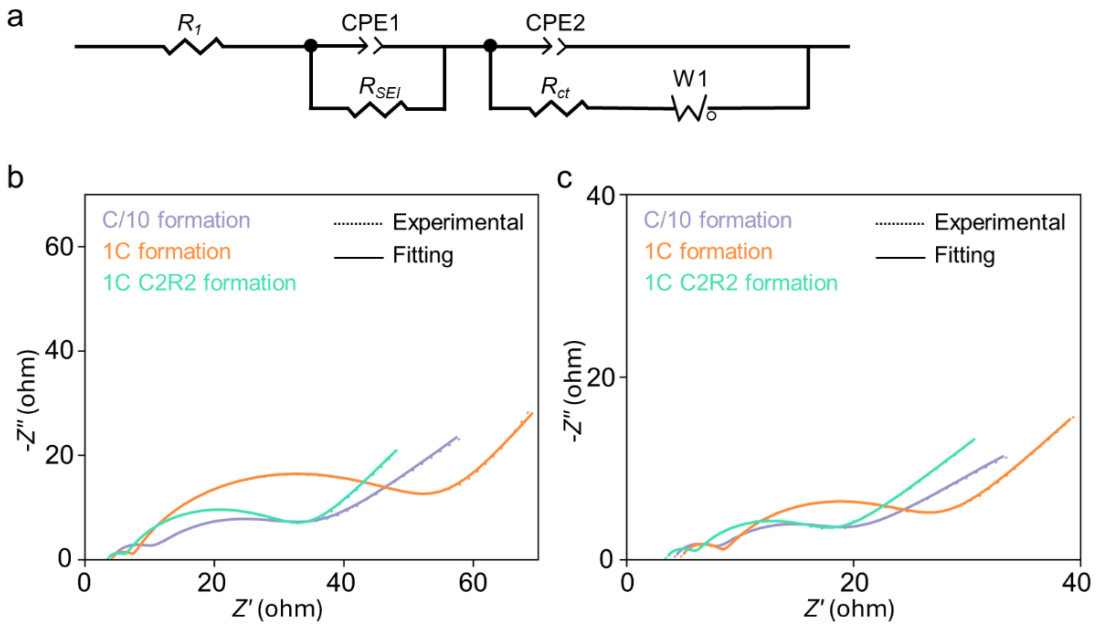

Fig. S17. a, Equivalent circuit model used for fitting the EIS data. b, Nyquist plots of LFP/graphite coin cells after different formation cycles (0.1C, 1C, and 1C C2R2), and c, after the first 1C cycle, both showing experimental data (dotted lines) and fitting curves (solid lines). Parameters: R_1: Electrolyte Resistance; R_{SEI}: SEI Resistance; R_{ct}: Charge Transfer Resistance; CPE1: Constant Phase Element 1; CPE2: Constant Phase Element 2; W1: Warburg Impedance.

Table S1 The fitted results of R_1, R_{SEI} and R_{ct} in LFP/graphite coin cells after different formation cycles (0.1C, 1C, and 1C C2R2), and after the first 1C cycle.

	0.1C formation	**1C formation**	**1C C2R2 formation**
After the formation cycle			
R_1 (Ω)	4.20	4.18	3.53
R_{SEI} (Ω)	5.61	3.08	2.53
R_{ct} (Ω)	23.79	47.22	27.28
After the 1st 1C cycle			
R_1 (Ω)	4.22	4.82	3.52
R_{SEI} (Ω)	3.52	3.48	2.38
R_{ct} (Ω)	10.98	18.84	11.93

To probe the chemical composition of the SEI formed under different formation protocols, XPS analyses were carried out on graphite electrodes after the formation cycle. Both survey spectra and high-resolution core-level spectra were collected to evaluate the elemental composition and chemical bonding states of the SEI. As shown in Fig. S18, the XPS survey spectra show an increased overall fluorine content under high-current formation, with the total fluorine atomic percentage increasing from 11.12 at% for the low-current case to 20.09 at% for the C2R2-formed SEI.

As shown in Figs. S19 and S20, the deconvoluted C 1*s* spectra can be assigned to five

major components: $ROCO_2Li$ (~289.8 eV), C=O (~289.0 eV), C–O (~286.7 eV), C–C (~284.8 eV), and C–Li (~282.0 eV). Despite broadly similar chemical species across all protocols, their relative concentrations vary with current density. At lower current (0.1C), the SEI contains higher fractions of organic species (C–O, C=O, $ROCO_2Li$), whereas at higher current (1C C2R2) these are suppressed. Consistent with the increased fluorine content observed in the survey spectra, the F 1*s* spectra (Fig. S20) indicate an enhanced contribution from LiF (~684.9 eV) under pulsed high-current formation.

Taken together, the survey-level fluorine enrichment and the core-level chemical analysis indicate that pulsed high-current formation promotes a more LiF-rich and inorganic-dominated SEI. The enrichment of LiF under pulsed high-current conditions is expected to facilitate faster Li^+ transport across the SEI and suppress parasitic reactions during cycling.

XPS depth-profiling (Fig. S21) reveals clear differences in SEI composition under different formation protocols. At 0.1C, the $–CO_3$ signal in C 1*s* spectra increases continuously with sputtering depth, while the Li–C peak only becomes evident after ~18 min, indicating a thicker organic-rich SEI with relatively low inorganic content. In contrast, under 1C C2R2, the Li–C signal emerges rapidly within 2–4 min and the $–CO_3$ content peaks near the surface but decreases with depth, suggesting a thinner SEI with a higher inorganic fraction. These results demonstrate that pulsed high-current formation yields a thinner, more inorganic-rich SEI, which is favorable for fast Li^+ transport and stable cycling performance. These results collectively demonstrate that high-current formation promotes the development of a thin, LiF-rich, and robust SEI layer.

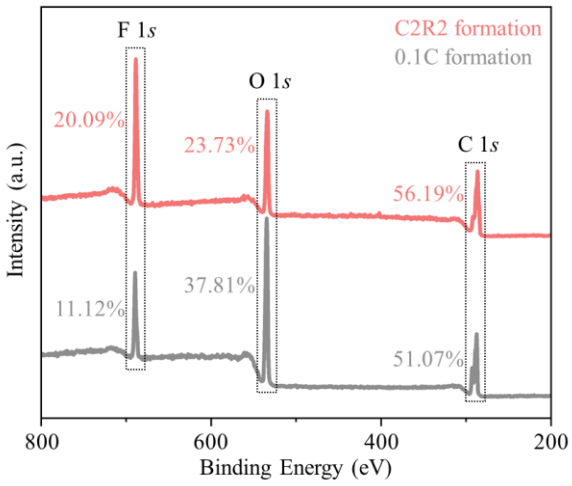

Fig. S18. XPS survey spectra of SEI on graphite anodes in LFP/graphite cells after 0.1C and 1C (C2R2) formation, with C, O, and F at%.

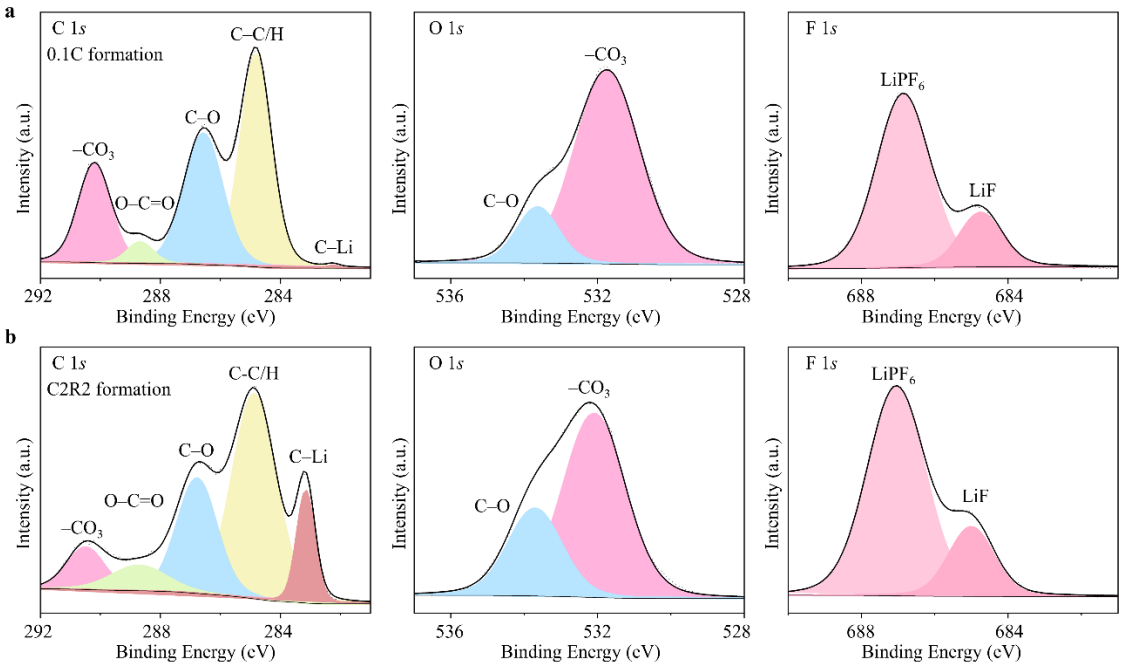

Fig. S19. XPS spectra of the SEI on graphite anodes in LFP/graphite coin cells after the formation cycle: a, under 0.1C formation and b, under 1C C2R2 formation.

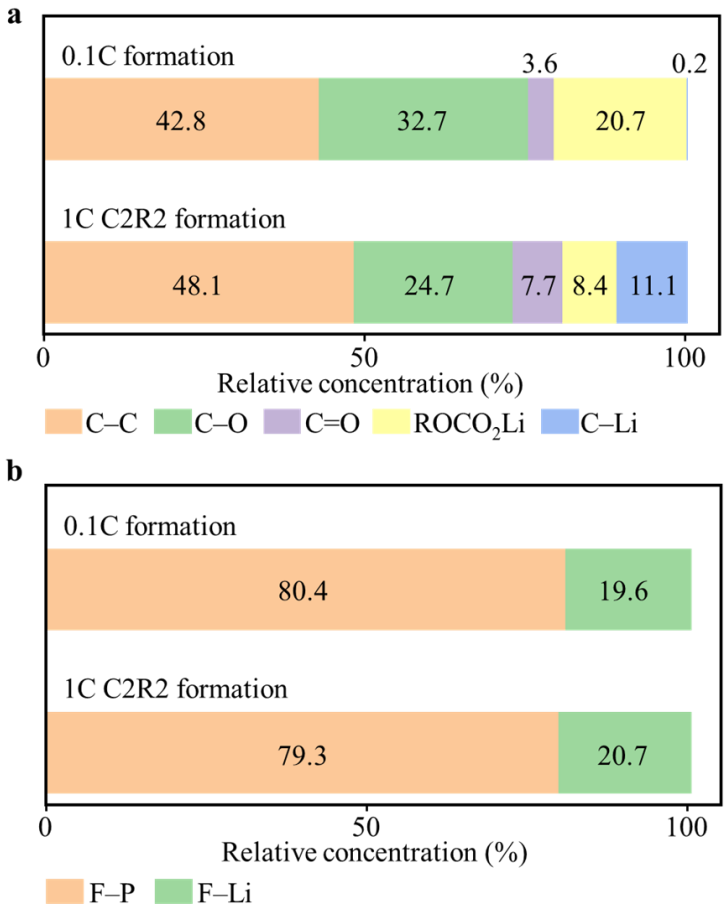

Fig. S20. a, Relative atomic ratio of C–C, C–O, C=O, $ROCO_2Li$, and C–Li based on C *1s* spectra; b, Relative atomic ratio of F–P, Li–F based on F *1s* spectra, for graphite anodes in LFP/graphite coin cells after the formation cycle.

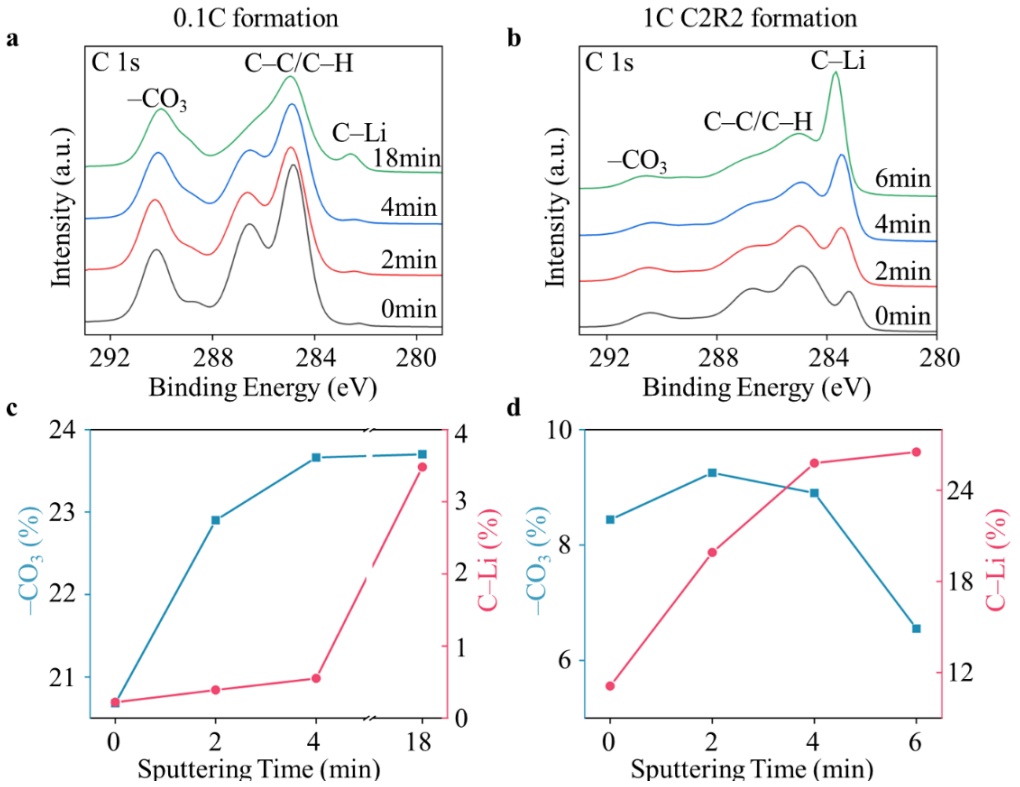

Fig. S21. XPS C 1*s* spectra and component evolution in the SEI on graphite anodes in LFP/graphite coin cells after the formation cycle. a, C 1*s* spectra under 0.1C formation; b, C 1*s* spectra under 1C C2R2 formation; c, quantitative changes in $–CO_3$ and Li–C content under 0.1C formation; d, quantitative changes in $–CO_3$ and Li–C content under 1C C2R2 formation.

6.2 Characterization of LIBs after aging

After 1000 cycles, post-mortem analyses were conducted using SEM and XPS to evaluate the SEI morphology and composition. As shown in Fig. S22 SEM images reveal that cells formed under the 0.1C protocol develop pronounced non-uniform, filamentary lithium deposition accompanied by surface deposits, indicative of aggravated side reactions. In contrast, cells formed under high-current protocols (e.g., 1C C2R2) retain a comparatively smoother graphite surface with no obvious filamentary lithium features. XPS (Figs. 23–24) further confirms these differences: the SEI formed at 0.1C contains a higher abundance of solvent- and salt-derived decomposition products., while high-current formation yields a more stable SEI that better preserves interfacial integrity after prolonged cycling.

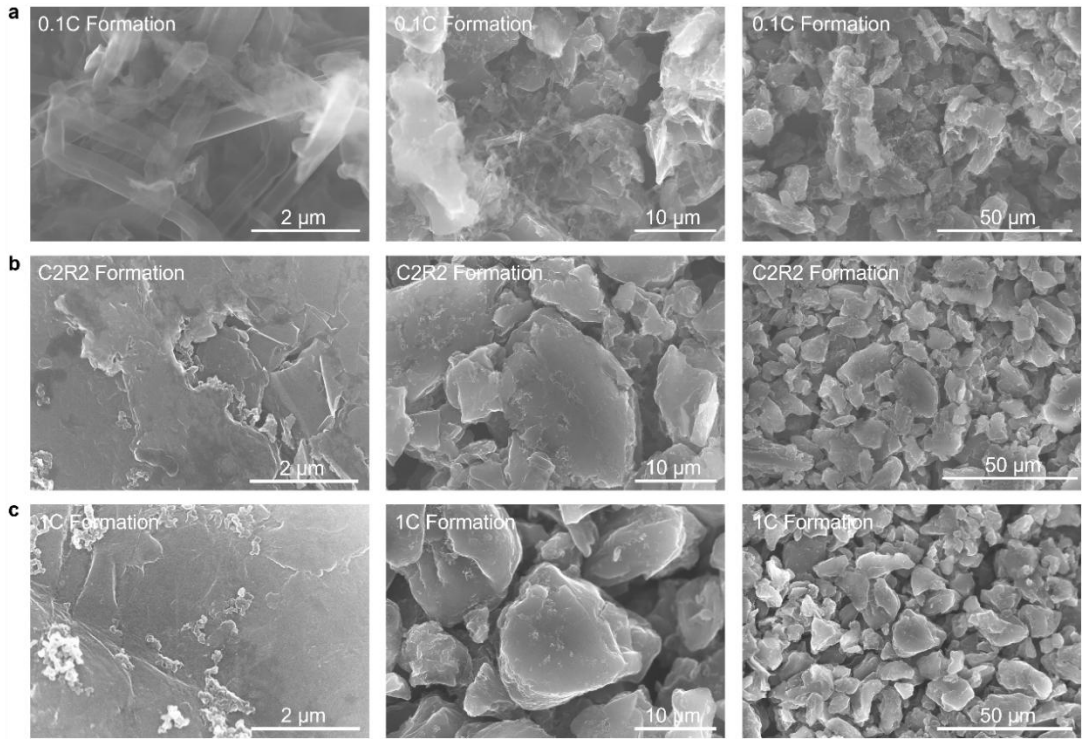

Fig. S22. SEM images of graphite anodes in LFP/graphite coin cells after 1000 aging cycles: a, 0.1C formation; b, 1C C2R2 formation; c, 1C formation.

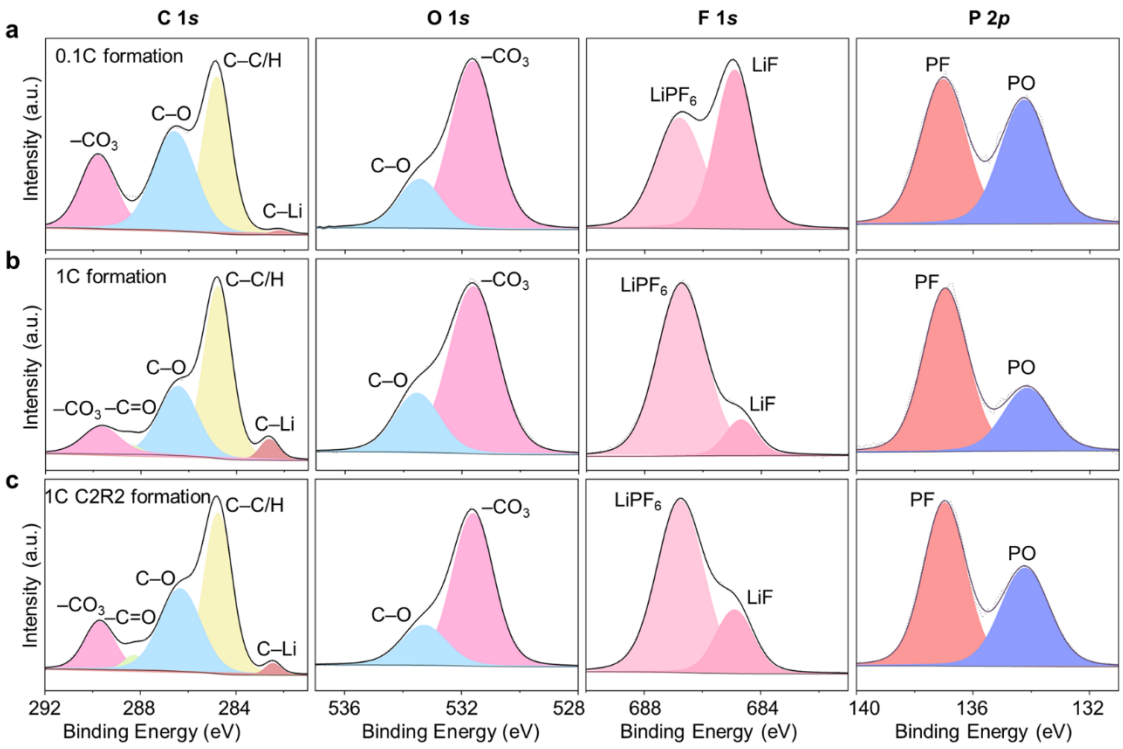

Fig. S23. XPS spectra of the SEI on graphite anodes in LFP/graphite coin cells after 1000 aging cycles: a, 0.1C formation; b, 1C formation; c, 1C C2R2 formation.

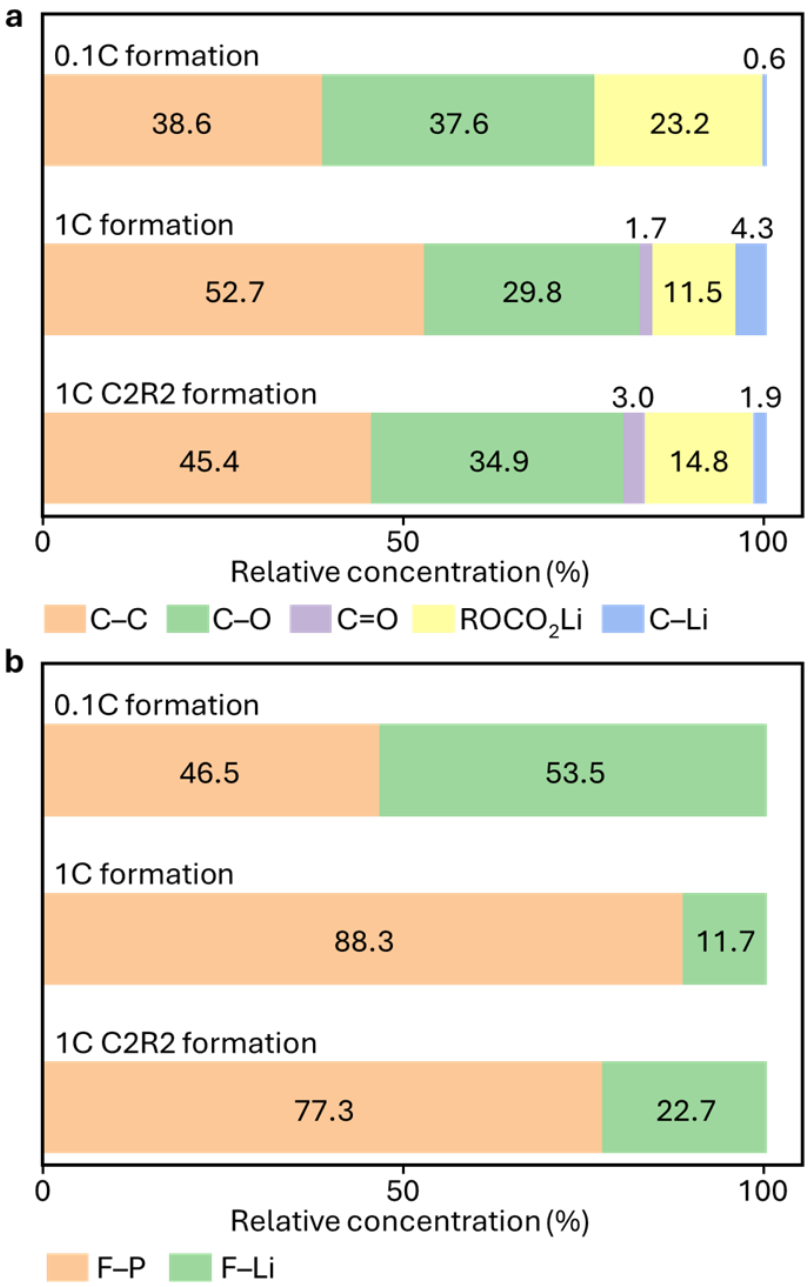

Fig. S24. a, Relative atomic ratio of C–C, C–O, C═O, ROCO2Li, and C–Li based on C 1s spectra; b, Relative atomic ratio of F–P, Li–F based on F 1s spectra, for graphite anodes in LFP/graphite coin cells after 1000 aging cycle.

6.3 Electrochemical data of LIBs formation under different protocols

Table S2 Detailed parameters of the 2.0 Ah LFP/graphite pouch cell.

Cathode	Materials	LFP
	Loading (%)	96.5
	Capacity (mAh/g)	142
	Press density (g/cc)	2.4
	Coating weight (mg/cm^2)	17.3
	Current collector thickness (μm)	15 with carbon coated
Anode	Materials	GA
	Loading (%)	95.7
	Capacity (mAh/g)	340
	Press density (g/cc)	1.5
	Coating weight (mg/cm^2)	8.8
	Current collector thickness (μm)	8
Cell Balance		1.2
Separator		16 μm PE + 4 μm Ceramic

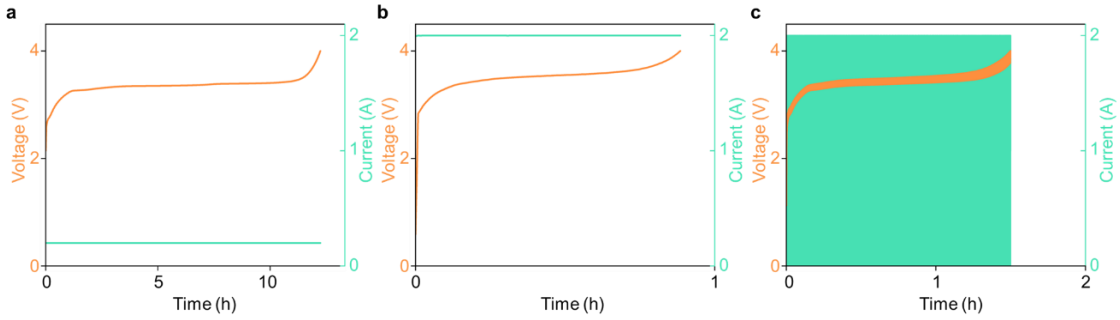

Fig. S25. Voltage, current and time profiles of 2 Ah LFP/graphite pouch cells during the first-cycle formation under different protocols. a, 0.1 C formation. b, 1 C formation. c, 1 C C2R2 formation.

Table S3 The formation time (i.e., the initial lithiation time) for different formation protocols in 2 Ah LFP/graphite pouch cells.

	0.1C formation	1C formation	1C C2R2 formation
Time (h)	12.27 ± 0.00	0.90 ± 0.01	1.46 ± 0.03

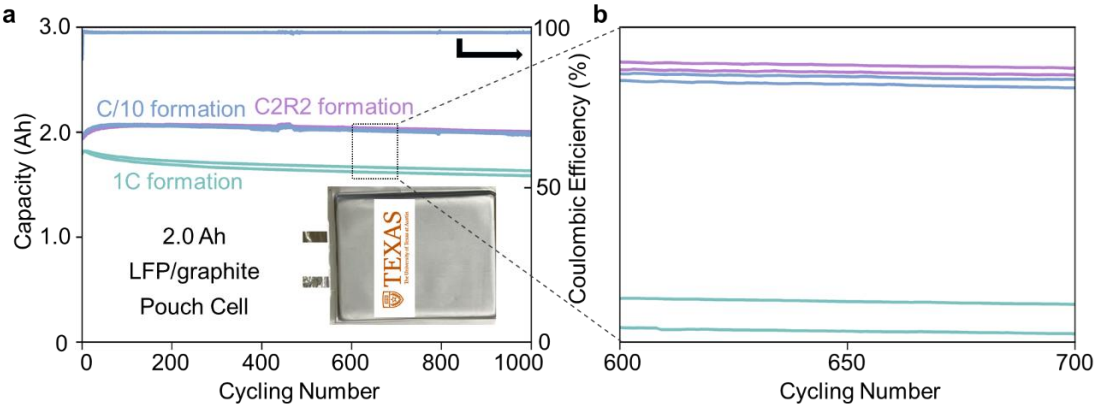

Fig. S26. Electrochemical performance of 2 Ah LFP/graphite pouch cells with different formation protocols. a, Capacity and Coulombic efficiency during cycling at 1C CCCV charge/1C discharge. b, Enlarged capacity curves for cycles 600–700. Each protocol was tested in duplicate.

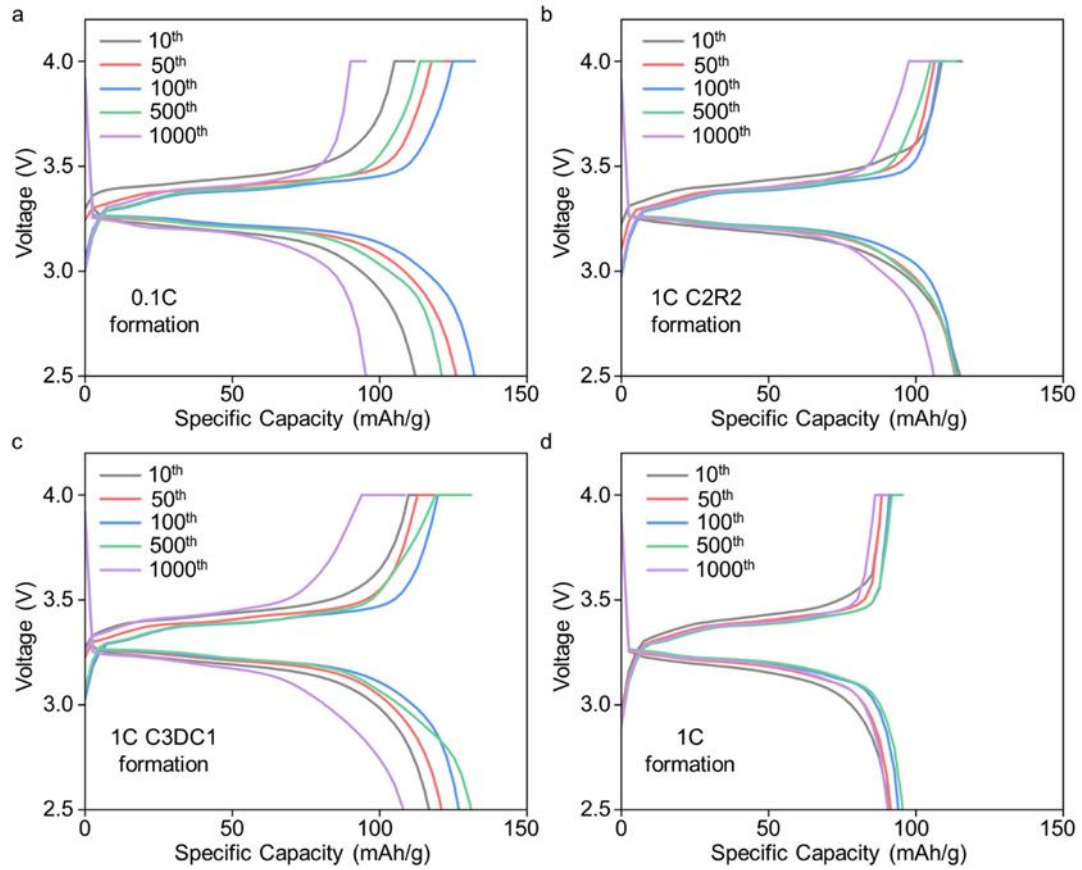

Fig. S27. Charge/discharge curves of LFP/Graphite coin cells under 1C CCCV charge and 1C discharge rate. Cells underwent different formation protocols: a, 0.1C formation; b, 1C C2R2 formation; c, 1C C3DC1 formation; d, 1C formation.

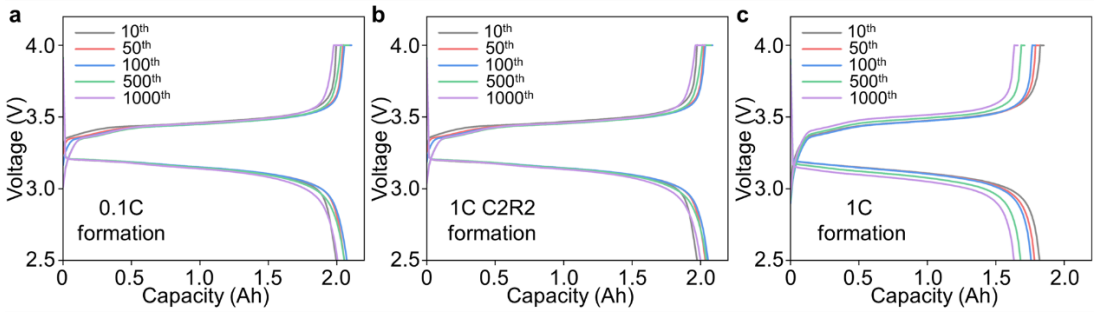

Fig. S28. Charge/discharge curves of LFP/graphite pouch cells under 1C CCCV charge and 1C discharge rate. Cells underwent different formation protocols: a, 0.1C formation; b, 1C C2R2 formation; c, 1C formation.

Supplementary Video 1

SEI formation dynamics during the first lithiation of a graphite/Li metal half-cell at C/20.

Supplementary Video 2

SEI formation dynamics during the first lithiation of a graphite/Li metal half-cell at C/10.

Supplementary Video 3

SEI formation dynamics during the first lithiation of an LFP/graphite full cell under pulsed 1C current.

References

1. E. Hecht, Optics. 4th edn addison-wesley. *Reading, Mass* (2002).
2. S. Cheon K. D. Kihm, Complex refractive index (RI) of graphene. *Handbook of graphene set* 389-412 (2019).
3. X. Wang, Y. P. Chen,D. D. Nolte, Strong anomalous optical dispersion of graphene: complex refractive index measured by Picometrology. *Opt. Express* **16**, 22105-22112 (2008).
4. P. Mineral Data, Zabuyelite (Li_2CO_3). *Handbook of Mineralogy* (2001).
5. E. Peled, The electrochemical behavior of alkali and alkaline earth metals in nonaqueous battery systems—the solid electrolyte interphase model. *J. Electrochem. Soc.* **126**, 2047 (1979).
6. F. Kong, R. Kostecki, G. Nadeau, X. Song, K. Zaghib, K. Kinoshita,F. McLarnon, In situ studies of SEI formation. *J. Power Sources* **97-98**, 58-66 (2001).
7. W. Youn, J. W. Lee, H. Yu,D. Y. Kim, Effect of refractive index contrast on out-coupling efficiency of corrugated OLEDs using low-refractive-index LiF interlayer. *ACS Appl. Electron. Mater.* **2**, 2218-2223 (2020).
8. M. A. McArthur, S. Trussler,J. R. Dahn, In Situ Investigations of SEI Layer Growth on Electrode Materials for Lithium-Ion Batteries Using Spectroscopic Ellipsometry. *J. Electrochem. Soc.* **159**, A198 (2012).
9. A. Nedjalkov, J. Meyer, A. Gräfenstein, B. Schramm, M. Angelmahr, J. Schwenzel,W. Schade, Refractive Index Measurement of Lithium Ion Battery Electrolyte with Etched Surface Cladding Waveguide Bragg Gratings and Cell Electrode State Monitoring by Optical Strain Sensors. *Batteries* **5**, 30 (2019).
10. Y. Chen, K.-H. Chen, A. J. Sanchez, E. Kazyak, V. Goel, Y. Gorlin, J. Christensen, K. Thornton,N. P. Dasgupta, Operando video microscopy of Li plating and re-intercalation on graphite anodes during fast charging. *J. Mater. Chem. A* **9**, 23522-23536 (2021).
11. J. B. Goodenough Y. Kim, Challenges for Rechargeable Li Batteries. *Chem. Mater.* **22**, 587-603 (2010).
12. J. Yan, J. Zhang, Y.-C. Su, X.-G. Zhang,B.-J. Xia, A novel perspective on the formation of the solid electrolyte interphase on the graphite electrode for lithium-ion batteries. *Electrochim. Acta* **55**, 1785-1794 (2010).
13. J. Yan, Y.-C. Su, B.-J. Xia,J. Zhang, Thermodynamics in the formation of the solid electrolyte interface on the graphite electrode for lithium-ion batteries. *Electrochim. Acta* **54**, 3538-3542 (2009).
14. J. Yan, B.-J. Xia, Y.-C. Su, X.-Z. Zhou, J. Zhang,X.-G. Zhang, Phenomenologically modeling the formation and evolution of the solid electrolyte interface on the graphite electrode for lithium-ion batteries. *Electrochim. Acta* **53**, 7069-7078 (2008).